SOLUTION SYNTHESIS AND ADDITIVE MANUFACTURING OF BISMUTH

TELLURIDE NANOFLAKES FOR FLEXIBLE ENERGY HARVESTING

by

Ariel E. Weltner

A thesis

submitted in partial fulfillment

of the requirements for the degree of

Master of Science in Materials Science and Engineering

Boise State University

August 2022

BOISE STATE UNIVERSITY GRADUATE COLLEGE

DEFENSE COMMITTEE AND FINAL READING APPROVALS

of the thesis or submitted by

Ariel E. Weltner

Thesis or Title: Solution Synthesis and Additive Manufacturing of Bismuth Telluride Nanoflakes for Flexible Energy Harvesting

Date of Final Oral Examination: 13 June 2022

The following individuals read and discussed the thesis submitted by student Ariel E. Weltner, and they evaluated the student's presentation and response to questions during the final oral examination. They found that the student passed the final oral examination.

David Estrada, Ph.D.   Chair, Supervisory Committee

Paul J. Simmonds, Ph.D.   Member, Supervisory Committee

Jessica E. Koehne, Ph.D.   Member, Supervisory Committee

Tony Varghese, Ph.D.   Member, Supervisory Committee

The final reading approval of the thesis was granted by David Estrada, Ph.D., Chair of the Supervisory Committee. The thesis was approved by the Graduate College.

DEDICATION

This thesis is dedicated to my husband, Alec, who has stood by my side since the very beginning and showered me with unconditional love and support, and to my sister, Heather, who paved the way and encouraged me at every step. Without you both I would have never had the courage to pursue an engineering degree. Finally, I would like to dedicate this thesis to the passionate, innovative, and ambitious women in higher education who are finding their voice, supporting each other, and tenaciously pursuing their goals.

ACKNOWLEDGMENTS

ABSTRACT

Flexible thermoelectric generators (TEGs) are energy harvesting devices which convert temperature differences into electrical power. These devices require no moving parts and offer silent and autonomous operation. The variety of suitable materials covering a broad range of operating temperatures positions TEGs as a promising renewable energy source using waste heat recovery, especially for space and microgravity applications. Conventional manufacturing of flexible electronic and thermoelectric devices requires complicated and relatively expensive processing, which limits the capabilities of in-space manufacturing. Additive manufacturing (AM) expands the use of flexible electronics to new surfaces, applications, and recently, low gravity conditions. Plasma jet printing (PJP) is a new AM modality in which material is deposited via a gravity- independent plasma. This thesis demonstrates solution processing, ink synthesis, and PJP of bismuth telluride (Bi_2Te_3) nanoflakes for low temperature energy harvesting. Synthesis conditions were tailored to control nanoflake morphology and ink processing was optimized for direct printing on flexible polyimide substrates. The thermoelectric films demonstrate promising thermoelectric properties, material adhesion, and flexibility, with only a 7.2% variation in performance after 10,000 bending cycles over a 16 mm radius of curvature. This advancement of Bi_2Te_3 solution processing and demonstration of PJP of thermoelectric films marks a significant contribution to in space manufacturing of flexible thermoelectric devices for wearable technology and low temperature energy harvesting.

TABLE OF CONTENTS

LIST OF TABLES

LIST OF FIGURES

LIST OF ABBREVIATIONS

TEG	Thermoelectric Generator
AM	Additive Manufacturing
PJP	Plasma Jet Printing
Bi_2Te_3	Bismuth Telluride
CO_2	Carbon Dioxide
CHP	Combined Heat and Power
ZT	Thermoelectric Figure of Merit
TE	Thermoelectric
η_C	Carnot Efficiency
T_H	Hot Side Temperature of Carnot Heat Engine
T_C	Cold Side Temperature of Canot Heat Engine
T	Temperature
S	Seebeck Coefficient
σ	Electrical Conductivity
κ_l	Lattice Thermal Conductivity
κ_e	Electron Thermal Conductivity
Pb	Lead
SiGe	Silicon Germanium
Bi	Bismuth
Te	Tellurium

Sb	Antimony
Se	Selenium
S	Sulfur
Cu	Copper
MOCVD	Metal Organic Chemical Vapor Deposition
NW	Nanowire
NP	Nanoparticle
PVP	Polyvinylpyrrolidone
EDTA	Ethylenediaminetetraacetic acid
Sb_2Te_3	Antimony Telluride
NaOH	Sodium Hydroxide
3D	Three Dimensional
ASTM	American Society of Testing and Materials
IJP	Inkjet Printing
AJP	Aerosol Jet Printing
CAD	Computer Aided Design
2D	Two Dimensional
DBP	Dielectric Barrier Discharge
Re	Reynolds Number
We	Weber Number
Oh	Ohnesorge Number
ρ_f	Fluid Density
η	Viscosity

v	Fluid Velocity
d	Drop or Nozzle Diameter
γ	Surface Tension
ρ_g	Gas Density
U	Jet Mass Flux
ρ_s	Gas Density Under Standard Conditions
Q	Volumetric Flow Rate of Gas
$Bi(NO_3)_3 \cdot 5H_2O$	Bismuth Nitrate Pentahydrate
Na_2TeO_3	Sodium Tellurite
IPA	Isopropanol
AFM	Atomic Force Microscopy
TEM	Transmission Electron Microscopy
SEM	Scanning Electron Microscopy
EDS	Energy Dispersive Spectroscopy
SLA	Stereolithography
ROC	Radius of Curvature
V	Voltage
I	Current
R	Resistance
VOC	Open Circuit Voltage
ΔT	Temperature Difference

CHAPTER ONE: INTRODUCTION

1.1 Motivation

Growing concerns over climate change, combined with increasing global populations and energy consumption, requires advancements in energy production which simultaneously provide high power density and minimal environmental impact. A study out of the Lawrence Livermore National Laboratory found that the United States consumed 92.9 Quads of energy in 2020.[1] Less than 1% of this energy consumption was produced via renewable sources such as solar, hydro, wind, and geothermal. In contrast, the most significant contributions were petroleum, natural gas, and coal, which accounted for 33%, 32%, and 9.4% of total U.S. energy production. These fossil fuel sources alone were responsible for 4,571 million metric tons of carbon dioxide, (CO_2), emissions in the United States in 2020 making it by far the most significant contributor to greenhouse gas emission.[2]

Out of the 92.9 Quads of energy produced in the United States in 2020 67% was rejected and returned to the environment due to inefficient energy conversion or use, such as energy lost as waste heat. Efforts to reduce rejected energy include making energy conversion more efficient via engineering and structural design, however this is limited by thermodynamic laws and the number of moving parts required in traditional power plants. Renewable energy resources, like those mentioned above, are promising alternatives but continue to suffer from high initial cost and weather dependency.[3] Another solution is to design devices capable of converting waste heat into usable

electricity during various stages in the energy life cycle, from production, to conversion, to final application. Thermoelectric generators (TEGs) are energy harvesters uniquely suited for waste heat recovery. TEGs provide direct conversion of temperature differences into electrical energy without the need for moving parts or intermediate processing stages.

Recently, TEGs have been applied in automotive engines[4-8], space shuttles and rovers[9-12], solar technology[13-16], wearable technology[17-20], and combined heat and power (CHP) systems[21-24]. Despite broad applications, TEGs demonstrate low conversion efficiencies in the range of $2 - 7\%$.[15, 16, 22, 24, 25] Routes for improving TEG performance include device design, increasing the temperature differential by optimizing TEG placement, appropriate thermoelectric material choice for the given application, and engineering thermoelectric (TE) materials for high figure of merit (ZT). Material design of thermoelectric materials for enhanced TE performance has been achieved by doping or alloying[26-30] and nanostructuring[26, 31-34] Despite these advancements further research is needed to develop thermoelectric materials and TEG fabrication methods to provide high efficiency and low cost devices.

TEGs by design operate by electrically connecting a n-type and p-type thermoelectric material and applying a heat differential across them, as shown in Figure 1.1. A TEG is a heat engine and as such the maximum efficiency is limited by the Carnot efficiency, $\eta_C = (T_H - T_C)/T_H$, which states that energy can only be absorbed from the difference in temperature between the hot side (T_H) and cold side (T_C) and not by ambient or background temperature. The performance of a TEG also depends on the dimensionless figure of merit $ZT = \frac{S\sigma^2 T}{\kappa_l + \kappa_e}$, which accounts for material properties of the

n- and p-type sides of the device and temperature (T). The interrelated properties of the
Seebeck Coefficient (S), electrical conductivity (σ), and lattice and electron contributions
to thermal conductivity (κ_l and κ_e) make it difficult to optimize one property without
negatively impacting the others, resulting in slow progress in increasing ZT.
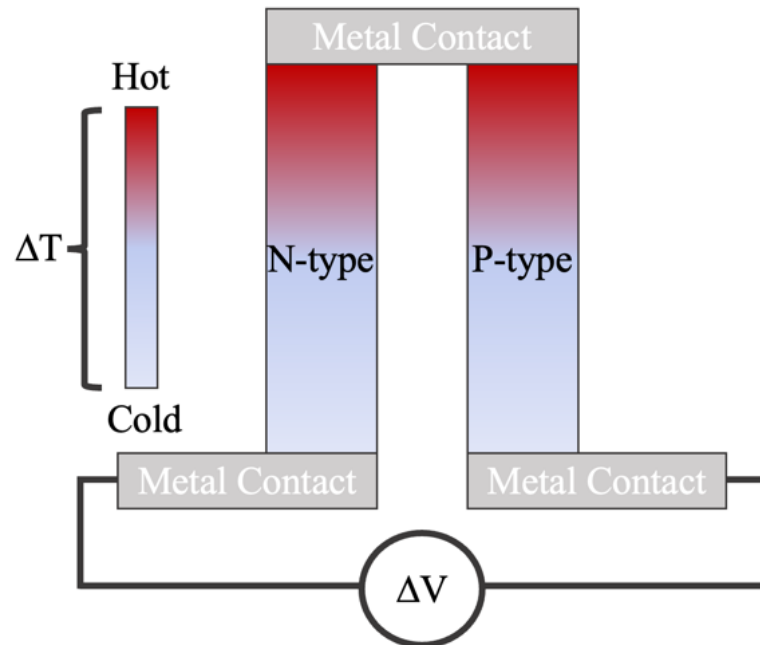
**Figure 1.1   Schematic of a temperature gradient across a TEG demonstrating
placement of the n- and p-type films connected by silver contacts**

Different TE materials demonstrate enhanced ZT within various temperature
ranges, as shown in Table 1.1. Bismuth telluride (Bi_2Te_3) based alloys demonstrate high
ZT at temperatures near room temperature, causing it to be well suited for applications in
cooling systems, wearable technology, and automotive engines. Lead (Pb) -based alloys
and skutterudites demonstrate enhanced ZT at intermediate temperatures and are suitable
for applications in engine exhausts and furnaces. High temperature thermoelectric
materials include half-Heusler and silicon germanium (SiGe)-based materials and would
be suited for refinement furnaces, hydrogen plants, and space reactors.

Table 1.1 **Reported ZT for Low, Medium, and High Temperature Thermoelectric Materials and Recommended Waste Heat Applications. Adapted from Zulkepli *et al.*[35]**

Temperature (K)	Material	ZT	Reference
Low (<400)	$Bi_2Te_{2.7}Se_{0.3}$- Bi_2S_3	0.49	[36]
	$Bi_2Te_{2.7}Se_{0.3}$	0.9	[37]
	$(Bi_{0.25}Sb_{0.75})_2Te_3$	0.92	[38]
	$MgAg_{0.97}Sb_{0.99}$	0.85	[39]
Medium (600 – 900)	$Na_{0.03}Eu_{0.03}Cd_{0.03}Pb_{0.91}Te$	~2.5	[40]
	Skutterudite ($Yb_yCo_4Sb_{12}$/ $Ce_yFe_3CoSb_{12}$)	1.5/ 1.06	[41]
High (>900)	Half-Heusler ($Zr_{0.5}Hf_{0.5}NiSn_{0985}Sb_{0.015}$/ $Zr_{0.5}Hf_{0.5}CoSb_{0.8}Sn_{0.2}$)	1.07/ 0.92	[42]
	SiGe-20%SiMo	0.79	[43]
	$SrTiO_2$- SiGe	0.91	[44]

1.2 Research Goals

NASAs recent In-Space Manufacturing initiative has motivated research for additive manufacturing (AM) of functional electronics. The Space Foundry plasma jet printer (PJP) provides a significant contribution to this initiative by enabling gravity-independent AM onto flexible and conformal substrates. As a result, a new research field opens in the development of PJP- compatible colloidal inks and simultaneous optimization of print and post-processing conditions of these inks onto various substrates and for various applications.

In addition, AM of TEGs for in-space energy harvesting has received research attention with applications ranging from radioisotope TEGs for powering various

instrumentation[9 – 12], to powering wearable sensors for monitoring astronaut's vital signs[18 – 20]. The scope of this research will focus on the development of low-temperature thermoelectric materials and films for wearable and flexible electronics and sensors.

This thesis addresses these research areas through the development of plasma jet printed thermoelectric films. The objectives of this research are: (1) synthesis of PJP-compatible thermoelectric inks and (2) demonstration of PJP thermoelectric films and optimization of post-processing of printed films for improved electric and thermoelectric performance.

Objective 1 includes the solutions synthesis of Bi_2Te_3 nanoflakes and development of a colloidal cosolvent ink system compatible with the PJP. This will include the optimization of nanoparticle size and a thorough understanding of ink properties impacting printability, such as viscosity and particle stability.

Objective 2 includes the post-processing of printed films by mechanical pressing and thermal sintering. The goal of these steps is to densify the films and increase contact between adjacent nanoflakes. The optimal thermal sintering condition will be determined by measuring the electrical conductivity and Seebeck Coefficient of the films.

CHAPTER TWO: BACKGROUND

2.1 Bismuth Telluride

Bi_2Te_3 is a semiconductor material belonging to the trigonal crystal system and

$R\bar{3}m$ [166] space group. The unit cell of Bi_2Te_3, shown in Figure 2.1a, corresponds to

one monolayer which consists of three van der Waals bonded quintuple layers. Each

quintuple layer is formed from an alternating sequence if bismuth (Bi) and tellurium (Te)

atoms in the order $Te^{(1)}$-Bi-$Te^{(2)}$-Bi-$Te^{(1)}$, where the (1) and (2) superscripts denote

inequivalent Te sites. The layered structure of Bi_2Te_3 and weak van der Waals bonds

between $Te^{(1)} - Te^{(1)}$ atoms results in anisotropy of electrical conductivity and lattice

thermal conductivity.
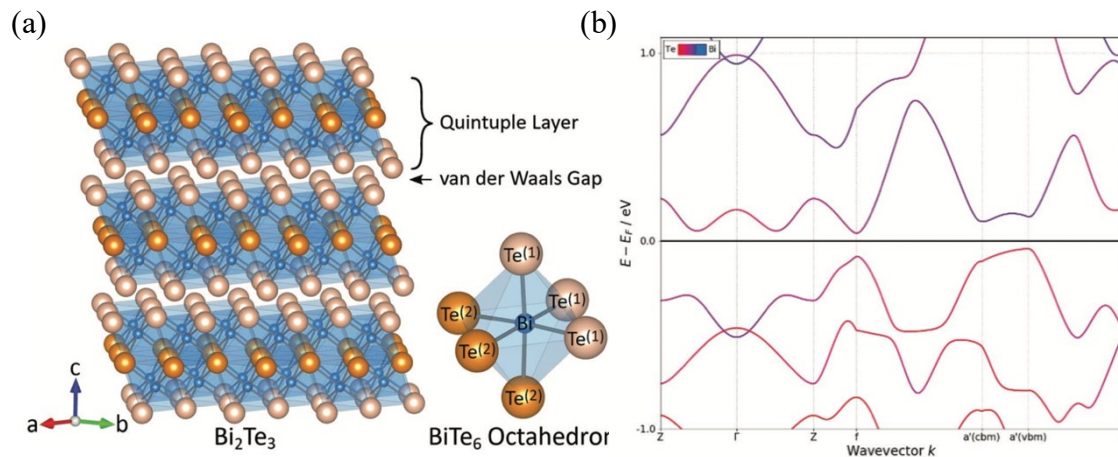
Figure 2.1 **Bi_2Te (a) unit cell and (b) band structure.**[45]

Bi_2Te_3 demonstrates intrinsically low lattice thermal conductivity, especially

across the van der Waals gap. In addition, Bi_2Te_3 demonstrates excellent electrical

properties due to its complex band structure. Spin-orbit interactions lower the energy of

Bi p-states below that of Te which produces band inversion at the Γ-point in the Brillouin

zone (Figure 2.1b). This interaction results in small bandgaps, small effective masses, and high valley degeneracy.

Material properties impacting ZT such as Seebeck coefficient and electrical conductivity may be tuned for optimized TE performance by alloying and doping telluride-based materials. Table 2.1 shows the alloying agent, composition, ZT possible for some common compounds.

Table 2.1   **Room Temperature Electronic and Thermoelectric Properties of Telluride and Selenide-Based Compounds**

Carrier Type	Compound	ZT	Reference
n-type	Bi_2Te_3 + 18 at% Cu	~0.46	46
	Bi_2SeS_2+0.01 CuI	~0.16	47
	$Bi_2Te_{2.71}Se_{0.3}$	~0.79	37
	Bi_2Te_2S	~0.45	48
p-type	$Bi_{1.95}Ge_{0.05}Te_3$	~0.95	49
	Sb_2Te_3	~0.24	50
	$Bi_{0.5}Sb_{1.5}Te_3$	~0.4	50

2.2 Bismuth Telluride Synthesis

Bottom-up synthesized nanostructures, such as nanowires (NW), nanoparticles (NP), and nanoflakes, have been intensely studied to take advantage of the quantum confinement effects of low dimensional materials.[26, 31 – 34] Electrodeposition and solvothermal or hydrothermal methods have been used to synthesize telluride-based nanostructures.[51 – 53] Electrodeposition is performed by using an electrical current to reduce cations of the desired material from an electrolyte to coat a conductive substrate

and has been used to form Bi_2Te_3 NWs using a metal coated alumina filter matrix as a template.[54]

Hydrothermal and solvothermal synthesis is performed by reducing precursor chemicals of the desired compound in either water or a solvent at elevated temperature. Capping agents such as polyvinylpyrrolidone (PVP) or ethylenediaminetetraacetic acid (EDTA) are commonly used to control nanostructure morphology during synthesis. The solution-based chemical reaction can take place in ambient or with a noble gas purge, in an autoclave, or sealed and placed in a microwave oven.[52, 53, 55] After synthesis, the solution is collected by an iterative rinsing process to remove the water or solvent and residual chemicals. An alcohol, such as ethanol, isopropanol, or acetone, is commonly added and the solution is centrifuged to form a pellet. The supernatant is poured off, more alcohol is added, and the solution is sonicated to break up the pellet. This process is repeated until all residual chemicals are removed. Finally, the collected pellet is either dried into a powder to press into a pellet or dispersed in a solvent for deposition onto a substrate.

The advantage of solvothermal or hydrothermal synthesis is the ability to control nanostructure size, shape, and morphology, which have direct correlations to properties impacting ZT. Zhang *et al.* observed a transition from NWs to nanoflakes in Bi_2Te_3 by varying the concentration and type of reducing agent and observed other morphology changes depending on capping agent type and synthesis time.[56] Im *et al.* observed a similar nanostructure transition from NWs to nanoflakes in antimony telluride (Sb_2Te_3) by changing the concentration of reducing agent sodium hydroxide (NaOH).[57] Akshay *et al.* observed optimization of ZT by varying synthesis time and EDTA concentration to

obtain various nanostructures.[58, 59] Solvothermal synthesis temperature was used by Hosokawa *et al.* to control formation of a single nanopore in the center of Bi_2Te_3 nanoflakes, which is predicted to enhance thermoelectric properties by reducing thermal conductivity via enhanced phonon scattering at the nanopore site.[60]

2.3 Additive Manufacturing

Additive manufacturing is a process by which objects or devices are fabricated one layer at a time based on a three-dimensional (3D) model. Two of the classifications of AM by the American Society of Testing and Materials (ASTM) include *material jetting* and *material extrusion*.[61] Material jetting refers to processes by which the 3D model is produced using a movable print head that deposits material either in a drop on demand or direct write approach. Inkjet (IJP), aerosol jet (AJP), and plasma jet (PJP) printers fall under this category. Material extrusion is a process by which a material is drawn through a nozzle, where it is then heated and then deposited onto a substrate. 3D printing is commonly performed by this method.

AM was developed in the 1980s, then known as Rapid Prototyping, as a method for developing models and prototypes based on 3D computer aided design (CAD) data.[62] Since then AM has been applied to industries which require low volume manufacturing of highly complex and customizable device designs. Applications have been found in the aerospace and automotive industry for metallic and polymer part fabrication[63 – 67], prototyping and modeling of complex anatomical parts in the medical industry[63, 67], and electronic and thermoelectric devices[68, 69].

AM has enabled the development of flexible and/ or wearable electronics beyond the capabilities of traditional subtractive manufacturing methods due to direct

manufacturing onto flexible, complex, and/or conformal surfaces. The design of flexible electronics and the ability to bend, roll, fold, and stretch expands the use of electronics onto new surfaces and applications beyond those available with traditional, rigid electronics.[70] Recent applications of AM of flexible electronics include photovoltaics[71, 72], sensors[73, 74], energy storage[75, 76], strain gauges[77], electrodes[78], and energy harvesters[79, 80].

Material Jetting Technologies

While the material deposition function of IJP, AJP, and PJP is unique, the general printing process involves the formulation of a nanomaterial-based ink that is deposited onto a substrate by passing through the printer nozzle. Advantages of material jetting processes include the ability to print complex structures and flexibility in changing designs from print to print by editing the computer programmed design file. In addition, these methods demonstrate minimal material waste due to the recyclability of unused ink after each print session.

IJP deposits material by holding ink in a cartridge or chamber and ejecting a fixed quantity onto a substrate by piezoelectric actuators in the printer nozzle, as shown in Figure 2.3a. Gravity pulls the droplet to the substrate, where it spreads based on the surface tension and fluid dynamics of the ink. Feature resolution of an IJP depends on the droplet size, ~30 μm for a Fujifilm Dimatix DMP 2850 printer.[81] AJP is a direct write technology in which the ink is held in a reservoir, where it is atomized by an ultrasonic bath and carried to the print nozzle by a carrier gas, such as nitrogen, as shown in Figure 2.3b. AJP offers the smallest feature size out of the three printer modalities of down to 10 μm.[82]

Both the AJP and IJP depend on gravity to deposit material which limits their use for device fabrication in low or zero gravity applications. Recently, Space Foundry has developed a printer modality in which the deposition mechanism is independent of gravity.[83] PJP deposits material via a helium gas plasma (Figure 2.2c) and has been shown to sinter metal nanoparticles *in situ*, reduce material oxidation states, promote substrate adhesion, and increase packing density.[84 – 86] The use of a dielectric barrier discharge (DBP) plasma in the PJP enables atmospheric printing of nanomaterial films without the need for expensive vacuum equipment. DBD plasmas have been shown to assist in etching and deposition of materials, modification of surface energy, and oxidizing, reducing, and removing organic films.[87, 88] Atmospheric plasma jets have been shown to operate more by electrical phenomenon than plasma flow, enabling high flow directionality that is independent of gravity.[88]

Recently, PJP of nanomaterial inks onto flexible substrates has been demonstrated with carbon nanotubes[85], silver nanowires[86], metal oxide nanoparticles[84, 89], and graphene oxide [90, 91]. The development of this new printing technology opens novel opportunities for integrating flexible energy harvesters in self powered electronic devices and marks significant progress in developing AM technologies for microgravity and space environments.
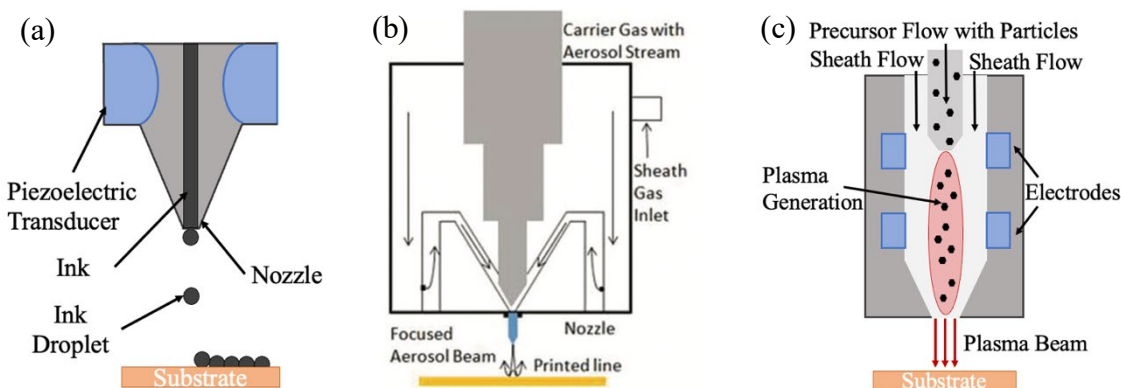
Figure 2.2 **Schematics of (a) inkjet printer, (b) aerosol jet printer[92], and (c) plasma jet printer printheads.**

2.4 Ink Synthesis and Rheology

The rheological properties of inks are important for understanding compatibility of nanomaterial inks with various printer modalities. The Reynolds (Re), Weber (We), and Ohnesorge (Oh) numbers relate various fluid properties to print conditions, such as nozzle or drop diameter and fluid velocity. While originally developed for inkjet printing, much work has been done recently to relate these values to other printer modalities, namely aerosol jet printing.[93 – 95]. The Reynolds number, $Re = \frac{\rho_f V d}{\eta}$, represents the ratio between inertial and viscous forces in a moving fluid and relates the fluid density (ρ_f) and viscosity (η) to the fluid velocity (v) and drop or nozzle diameter (d). Similarly, the Weber number, $We = \frac{\rho_f v^2 d}{\gamma}$ represents the ratio between the inertia and surface tension (γ) of the ink on a given substrate. The Ohnesorge, $Oh = \frac{\sqrt{We}}{Re} = \frac{\eta}{\sqrt{\gamma \rho d}}$, number combines these values to reflect only the physical properties of the ink scaled to the drop size, and is independent of velocity. Evaluation of these parameters combined with observations of inkjet drop formation allowed for researchers to identify the fluid parameters required for inkjet-printable inks, as shown in Figure 2.4.[96, 97]
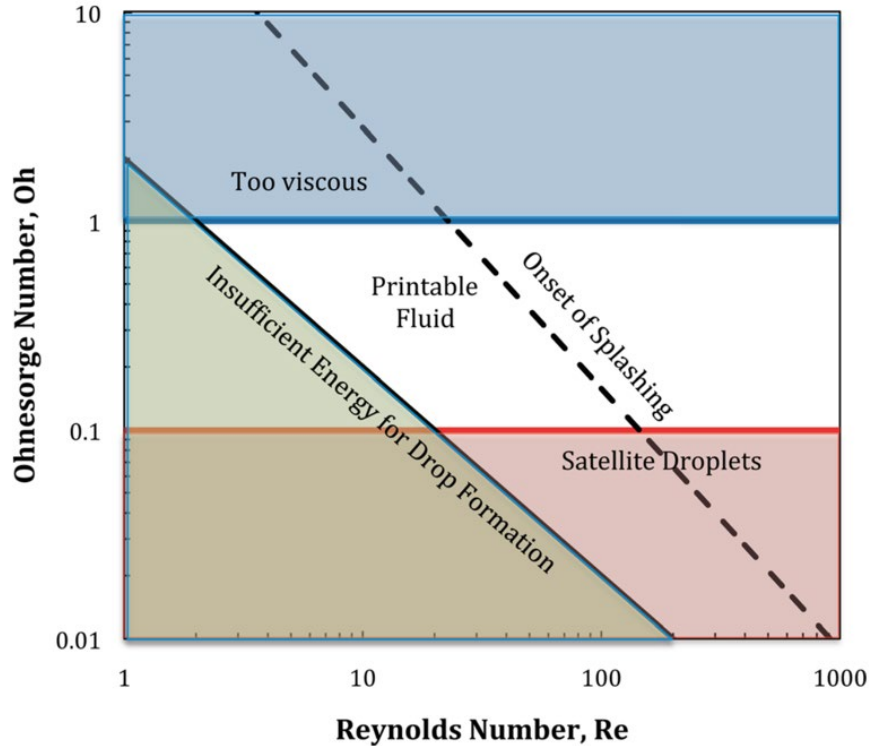
Figure 2.3   Schematic demonstrating the ink requirements for printable drop-on- demand inkjet printing.[97]

While these values are very effective in predicting printability of inks for drop-on- demand inkjet printers they have limited accuracy for predicting ink printability for aerosolizing modalities like aerosol jet or plasma jet printing. The Reynolds number can be adapted for aerosolization of particles and sheath gas deposition by replacing the fluid density with the gas density (ρ_g), and the fluid velocity with the jet mass flux $U = \frac{4\rho_s Q}{\rho_g \pi d^2}$, where ρ_s is the gas density under standard conditions and Q is the volumetric flow rate of the gas as measured on the printer by a mass flow controller.[94, 95] While PJP is similar to AJP in terms of aerosolization of particles the plasma- based deposition complicates the direct application of the IJP or AJP Reynolds number. While some reports have shown calculation of Reynolds number for PJP system more work is needed

to accurately account for the effect of plasma on jet velocity, density, and viscosity. [98–101]

CHAPTER THREE: METHODS

3.1 Chemicals

Bismuth nitrate pentahydrate ($Bi(NO_3)_3H_2O$, >99.9%), sodium tellurite (Na_2TeO_3, >99.5%), sodium hydroxide (NaOH, >99%), poly(vinyl) pyrrolidone (PVP, MW 40,000) and ethylene glycol were purchased from Fisher Scientific. All chemicals were used as received.

3.2 Solution Synthesis of Bi_2Te_3 Nanoflakes

Nanoflake synthesis was performed following work by Hollar *et al.*[92] In a standard reaction, 0.2 mmol $Bi(NO_3)_3H_2O$ (0.0970 g), 0.3 mmol Na_2TeO_3 (0.0665 g), 4 mmol NaOH (0.1600 g), and 2 mmol PVP (0.2223 g) were combined with 10 mL ethylene glycol in a 25 mL double neck flask. The mixture was stirred for 15 minutes using a magnetic stir bar to fully dissolve all solids before equipping with a reflux condenser and heating in an oil bath to 190˚C. After three hours the flask was removed from the oil bath and allowed to cool to room temperature naturally. 20 mL isopropanol (IPA) and 10 mL acetone was added to the mixture, followed by centrifugation at 20,000 RPM (37560 g) for 16 minutes at 20˚C. The supernatant was discarded, and the collected solids were redispersed in IPA by bath sonication. The washing steps were repeated two more times to remove excess ethylene glycol, PVP, and other impurities. The final product was dried over a hot plate and massed before dispersing in a water based co-solvent system to form the colloidal ink.

3.3 Plasma Jet Printing and Thermal Sintering

Thermoelectric ink was printed and sintered in collaboration with Jacob Manzi and Tony Varghese using a commercial helium PJP from Space Foundry (Model #sfas000000074 28). The TE ink was deposited onto polyimide (Kapton®) substrates that had been wiped with IPA. Print parameters, including printed layers, print speed, sheath and precursor gas flow, and plasma power were optimized during each session of printing for good adhesion, sufficient film thickness, uniform coverage, and minimal overspray. After printing the films were dried on a hot plate in ambient atmosphere at $150°C$ for one hour to remove any remaining ink solvent. Thermal sintering was performed in a commercial tube furnace in an inert atmosphere. The films were sintered for 60 minutes at various peak temperatures to optimize film quality and thermoelectric performance. The purpose of sintering is to remove ink solvents and capping agents from synthesis and induce grain growth within the film.

3.4 Nanoflake and Ink Characterization

Atomic Force Microscopy

Bi_2Te_3 nanoflakes were imaged using a Bruker Dimension Icon atomic force microscope (AFM) under atmospheric conditions. Imaging was performed using a ScanAsyst-Air probe (Bruker, 2 nm radius of curvature) operating in PeakForce Tapping mode. Thirty nanoflakes were imaged to derive statistics. The height of each nanoflake was recorded as the peak value from the substrate, excluding any particulates present. Width measurements were obtained for each of the three pairs of sides on the hexagonal nanoflake and averaged to report the lateral dimensions.

Transmission Electron Microscopy

Bi_2Te_3 nanoflake ink was diluted in IPA and mixed using ultrasonication. The dispersion was drop casted onto a 300-mesh carbon coated copper transmission electron microscope (TEM) grid for characterization using a JEOL 2100 HR TEM operating at 200 kV. Brightfield and high-resolution imaging was performed on the sample.

Ink Rheology

Surface tension and contact angle were measured using a Biolin Scientific Attension optical tensiometer. Viscosity was measured using a Brookfield Ametek rheometer. Both measurements were performed for each cosolvent system with a particle concentration of 20 mg/mL.

3.5 Printed Film Characterization

Scanning Electron Microscopy

Scanning electron microscopy (SEM) was used to image the topography of the as printed and pressed and sintered films. A Field Emission SEM (FEI Teneo) under high vacuum was used for imaging Both the ETD and T1 detectors were used to obtain varying resolution in imaging the deposited material.

Flexibility Testing

The mechanical flexibility and durability of the films after bending were tested using a custom built automated flexibility testing machine. The printed film was placed on a supporting piece of polyimide and repeatedly bent at a set radius of curvature (ROC). The electrical resistance of the films was measured and recorded in intervals to determine the impact of bending on film durability and adhesion to the substrate.

Electrical Testing

Electrical conductivity measurements were performed using a linear four-point probe method with an inner probe spacing of 6mm. A 100 mA current was passed through the sample and five measurements were taken of the voltage difference between the center probes. The resistance was calculated using Ohm's law, $V= IR$, where V, I, and R are the voltage, current, and resistance, respectively. The conductivity was calculated using the average thickness and width as measured by stylus profilometry to find the cross-sectional area.

Thermoelectric Property Testing

Seebeck Coefficient, and V-I and power measurements were performed on a custom test bed built using two commercial Peltier modules, one operating as heater and other as a cooler. The hot side and cold side of the TE film were thermally grounded to the Peltier modules to create a temperature gradient. Two E- type thermocouples were mounted with voltage probes on to the hot side and cold side with soft indium contacts to measure the temperature and voltage. An insulating layer was used to thermally insulate and apply pressure at the thermocouples for better contacts and measurements. The device was connected electrically in series to a shunt resistor and a variable resistor for impedance matching at each measurement temperature. The open circuit voltage, load voltage, current and power output from the device were measured for various applied temperature differences.

CHAPTER FOUR: RESULTS AND DISCUSSION

4.1 Nanoflake and Ink Synthesis

Figure 4.1a shows the solvothermal synthesis setup used to synthesize Bi_2Te_3 nanoflakes, following work performed by Hollar *et al.*[92] After washing the nanoflakes were dispersed in a cosolvent solution consisting of ethylene glycol, nanopure water and an alcohol (Figure 4.1b) for printing or spin coating onto various substrates, such as SiO_2 or polyimide.
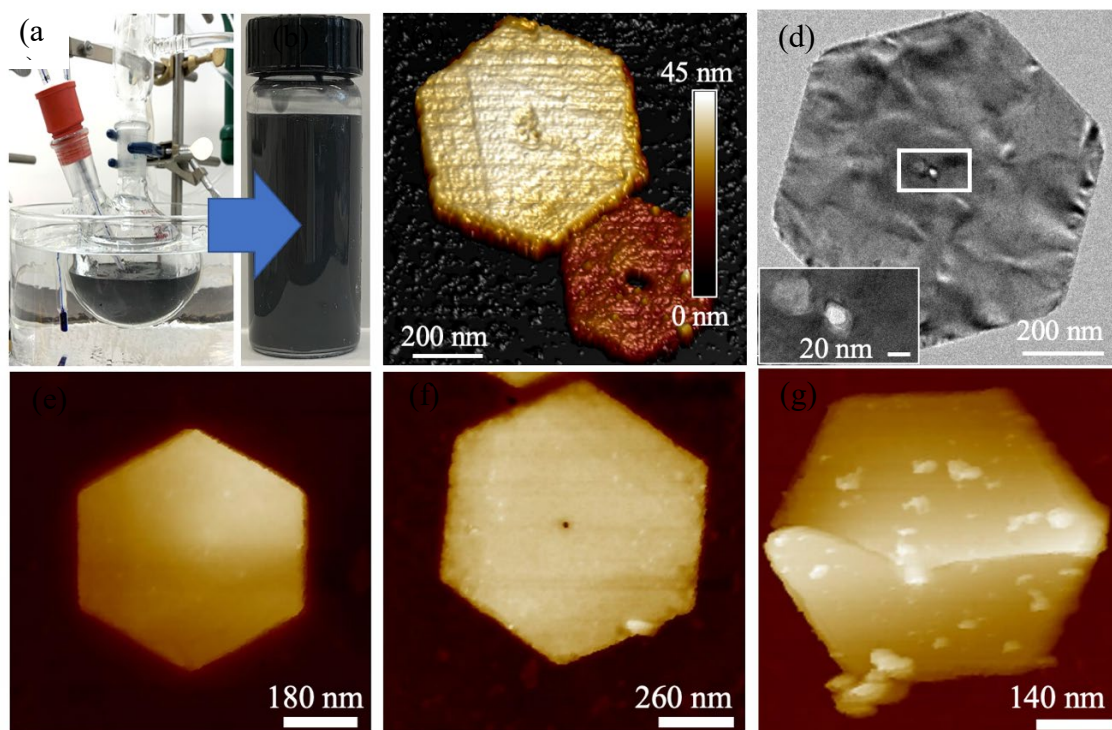
Figure 4.1 **Synthesis and characterization of Bi_2Te_3 nanoflakes. Optical images of (a) solvothermal synthesis process and (b) as-synthesized thermoelectric ink dispersed in the cosolvent system. (c) 3D rendering of a pair of nanoflakes showing surface morphology and (d) TEM images of a nanoflake showing a single nanopore. Representative AFM images of Bi_2Te_3 nanoflakes with (d) crystalline morphology, (e) single nanopores, and (f) dislocations.**

Nanoflakes were synthesized at 190˚C to form a single nanopore in the center of the nanoflake following work by Hosokowa *et al.*[60] The TEM and AFM images in Figure 4.1c -g show nanoflake morphology, including crystalline, single nanopores, and dislocations. The 3D rendering of a pair of flakes in Figure 4.1c show a triangular growth region in the center. Subrati *et al.* observed a similar feature and observed a growth mechanism in which nanoflakes form out of a Bi-rich triangular nuclei centered on a Te nanorod.[102]

Histograms of thickness and width are shown in Figure 4.2 a, b. From the AFM images the average thickness and width of nanoflakes are observed to be ~59 nm and ~598 nm, respectively. The yield of nanoflakes with nanopores is observed to be ~13% and the average nanopore diameter is ~64 nm.
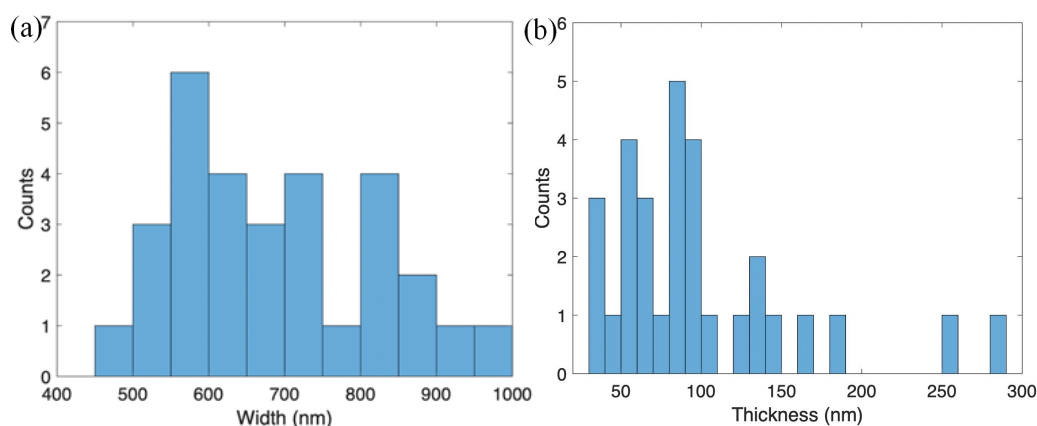
Figure 4.2   Histograms of (a) lateral width and (b) thickness of as-synthesized Bi$_2$Te$_3$ nanoflakes.

The rheological properties of Bi$_2$Te$_3$ dispersed in the cosolvent ink were extensively studied and compiled in Table 4.1. The alcohol component of the cosolvent system was varied to determine the optimal cosolvent composition. The alcohols are present in the exact same ratio compared to the other co-solvent chemicals. The cosolvent

system containing ethanol demonstrated superior stability compared to the other ink

composition, as indicated by the nanoparticles staying dispersed in solution even after

one week while the other cosolvent inks had sedimented completely (Figure 4.3)

Table 4.1   **Rheological properties of various inks. The ratio of water to ethylene glycol to alcohol is the same for each composition.**

	Water: ethylene glycol: ethanol	Water: ethylene glycol: isopropanol	Water: ethylene glycol: 2-butanol
Mean Contact Angle (˚)	48.49	41.31	19.14
Mean Viscosity (cP)	2.648	2.912	2.985
Surface Tension (mN/m)	37.05	33.52	27.18

The viscosity and surface tension of the various inks in Table 4.1 are similar and

all within the allowed parameters of the PJP. In comparison the mean contact angle varies

greatly with alcohol type. Due to the method of printing the high contact angle of the ink

is not a barrier, however further tuning of the ink composition would be necessary to

make the cosolvent system compatible with drop-on-demand printing modalities, such as

IJP which requires contact angles of 20-30˚.

isopropanol, and (d) 2-butanol.
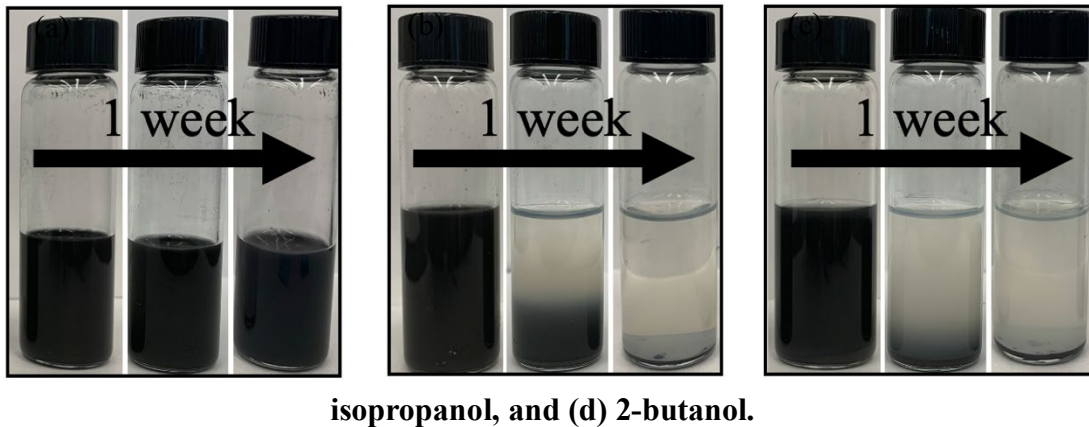
Initially, printing was conducted using the ink as- prepared ink with no further processing steps. However, it was quickly observed that the printhead clogged after 5-10 minutes and needed to be cleaned before printing could continue. Centrifugation processing of the ink was used to mitigate nozzle clogging by sedimenting out the largest nanoflakes and collecting the supernatant for printing.
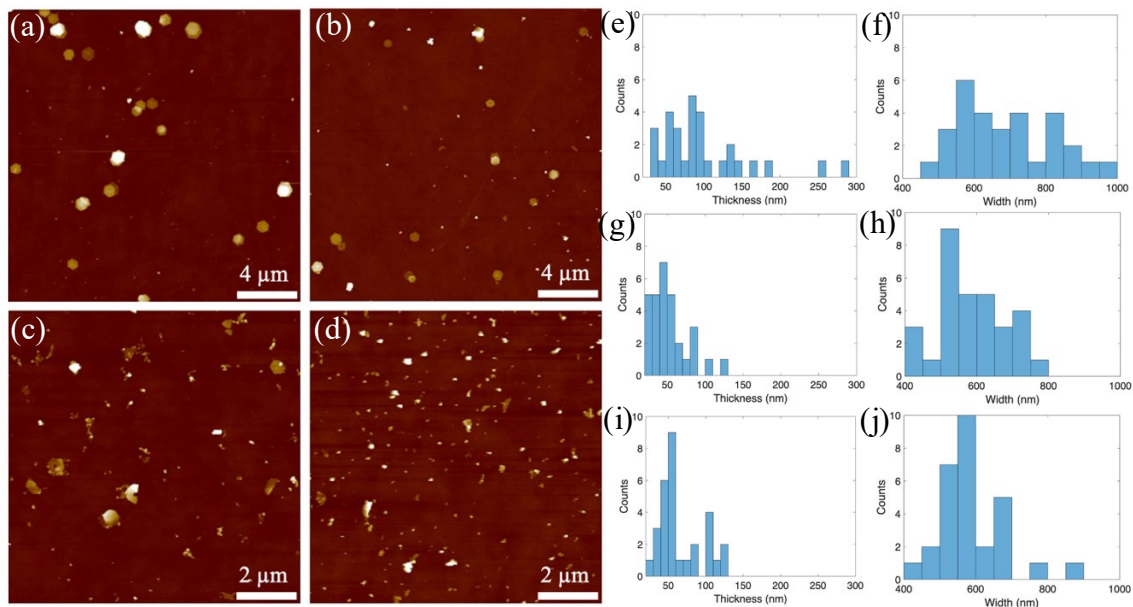
Figure 4.4   AFM images of inks formulated after (a) no centrifugation, (b) 3 minutes at 3000 RPM centrifugation, (c) 3 minutes at 4500 RPM centrifugation, and (d) 10 minutes at 4500 RPM, and width and thickness histograms for (e, f) no centrifugation, (g, h) 3 minutes at 3000 RPM centrifugation, (i, j) 3 minutes at 4500 RPM centrifugation.

Figure 4.4 shows AFM images and lateral width and thickness histograms for inks centrifuged at various speeds and times. To begin, centrifugation was performed for 10 minutes at 4500 RPM and the supernatant was collected for printing. The printer nozzle did not clog during printing however several print passes were required to achieve a comparable thickness to the prints using the as-synthesized ink. Further, these printed films showed a minimal change in resistance after sintering. The poor print quality and electrical performance can be explained by the lack of nanoflakes as observed by AFM (Figure 4.4d) where the ink appears to be mostly comprised of broken or not fully formed nanoflakes.

The centrifugation time was reduced to 3 minutes at 4500 RPM to reduce print time and improve film quality. As a result, the average nanoflake thickness and width were reduced to 55.54 nm and 579 nm. This formulation resulted in nanoflakes in the supernatant (Figure 4.4c) and an acceptable amount of print time before nozzle clogging, but the post-sintering film quality remained underwhelming. The final formulation was to maintain the centrifuge time at 3 minutes but reduce the centrifuge speed to 3000 RPM. This ink formulation shows a slight reduction in thickness to 51.15 nm and a similar nanoflake width to the formulation prior of 595 nm. The print time before nozzle clogging remained within an acceptable range and the post-sintering conductivity indicates good film quality, as supported by the increase in fully formed flakes (Figure 4.4b).

4.2 Plasma Jet Printing of TE Films

A Space Foundry PJP was used to print the TE films onto polyimide substrates. A schematic of the print head is shown in Figure 2.2c. The cosolvent Bi_2Te_3 is held in a

reservoir on the printer and atomized into a glass chamber by an ultrasonic mesh. Helium precursor gas carries the atomized particles into a secondary chamber, where larger droplets collect on the bottom or sides of the chamber and smaller droplets are directed to the printhead as a mist. The removal of large droplets in the secondary chamber aids in achieving a uniform size distribution of droplets in the printhead.

The precursor gas brings atomized particle to the printhead, where it is joined by a sheath gas of the same type in an optimal ratio of ~1:3.5 precursor to sheath flow. The plasma is generated from the combined precursor and sheath gas in a ceramic chamber surrounded by an alternating current and ground electrode. A high voltage (10-30 kV) and low frequency (20-30 kHz) power supply is used for plasma generation. The resonant frequency of the plasma is determined by manufacturer specifications and is used for the duration of the print time. The plasma power supply voltage, atomizer power, line spacing, and print speed are tailored *in situ* to optimize print quality.

The precursor flow rate controls the concentration of atomized particles that are deposited onto the substrate and must be optimized to achieve uniform prints while avoiding nozzle clogging. Too high of a flow rate results in a high concentration of particles and potential for nozzle clogging, while too low of a flow rate deposits a small concentration of particles and may increase the total print time and number of required layers to achieve a desired thickness. For this work a precursor flow rate of 100 – 120 sccm was used.

The sheath flow rate combines with the precursor flow in the printhead to generate the plasma. The flow range of the sheath gas was chosen to optimize film thickness and line quality and minimize overspray. When the sheath flow is too low the

printed line becomes very wide due to overspray and when the sheath flow is too high the line width decreases, and the deposited material does not adhere well to the substrate. A sheath flow of 350 – 400 sccm was used for this work to minimize overspray and achieve a uniform film thickness.

4.3 Thermal Sintering and Electrical and Thermoelectric Testing of TE Films

TE films with dimensions of 2 x 12 mm were printed onto polyimide substrates to test electric and thermoelectric properties. An optical image of the as-printed films is shown in the inset of Figure 4.5a. Figure 4.5a, b show top down and cross sectional SEM images of the as-printed films. Mechanical pressing was performed following work by Hollar *et* al, who observed a decrease in Seebeck Coefficient and electrical conductivity in AJP printed Bi_2Te_3 films compared to spin coated films due to increased porosity and random stacking of nanoflakes in as-printed films.[92] The recommendation of that work was to use compaction to improve performance. Figure 4.5 c, d show top down and cross sectional SEM images of the films as-printed and after pressing and sintering. Visible compaction is observed from the images and the thickness of the film reduced from ~10 µm to ~3-5 µm.
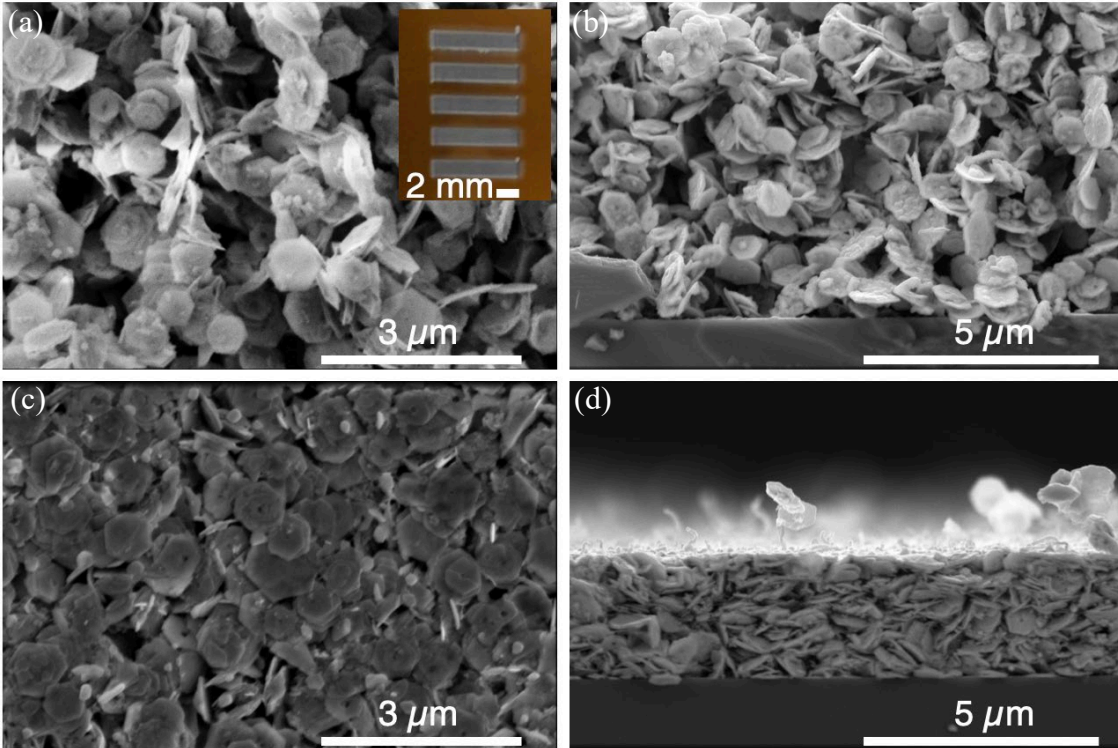
Figure 4.5   SEM imaging showing as-printed films (a) top down and (b) cross section and pressed and sintered films (c) top down and (d) cross section. Inset of (a) shows as printed Bi$_2$Te$_3$ on polyimide. Image Credit: Jacob Manzi

The printed films were thermally sintered for 60 minutes at four temperatures from 350 – 425˚C in the presence of a forming gas. Figure 4.6a, b shows the Seebeck coefficient and electric conductivity of the films measured at room temperature. A peak Seebeck coefficient of -162 µV/K was observed at a sintering temperature of 425˚C. The negative Seebeck Coefficient is consistent with the n-type behavior of the films. The Seebeck Coefficient shows little variation with sintering temperature, ranging from -144 µV/K to -162 µV/K. The introduction of single nanopores in the center of the nanoflakes and centrifugation size processing appears to improve the room temperature Seebeck coefficient and achieving a value comparable with doped Bi$_2$Te$_3$ nanoflakes.[103]

A maximum electrical conductivity of 2303 S/m was observed at a sintering temperature of 425˚C. Unlike the Seebeck coefficient, the electrical conductivity appears to vary greatly depending on the sintering temperature. The power factor ($S^2\sigma$), taken from the numerator of ZT, is shown in Figure 4.6c. These films demonstrated a peak power factor of 60. 5 m·K^2 at 425°C.
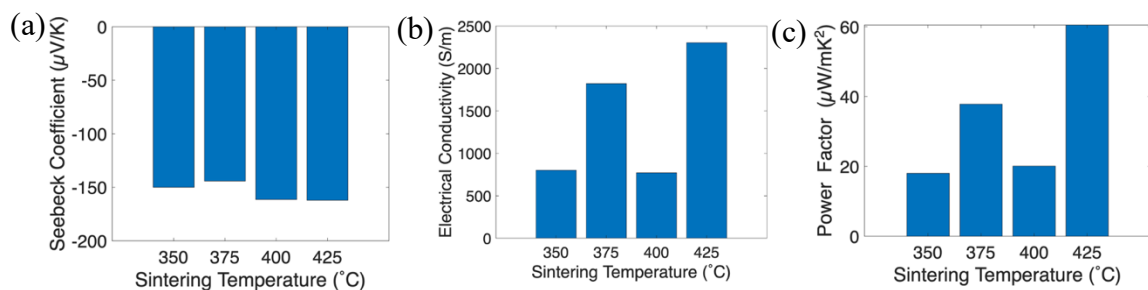
Figure 4.6   Room temperature (a) Seebeck Coefficient, (b) electrical conductivity and (c) power factor ($S^2\sigma$) after thermal sintering.

The measured electrical conductivity is an order lower than that of conventional bulk Bi_2Te_3 measured at room temperature and results in correspondingly low power factor. The low values may be explained by observing the cross-section SEM image in Figure 4.5d, which show high porosity within the film even after pressing and sintering. The high porosity of the films results in high interface resistance and low electrical conductivity. The porosity of the film is due to the random orientations and stacking of the nanoflakes on the substrate and the trapping of burn-off residues from the polymer capping agent. The low electrical conductivity and power factor may also be explained by the low sintering temperature, which is limited by the melting point of the polymer substrate.

Analysis of the porosity of the films before and after pressing and sintering was performed to quantify the impact of post-processing. Gwyddion software was used to threshold map the SEM images of the film cross sections shown in Figure 4.5 b, d. The

threshold mask was set to 20% and the relative area function was used to find percentage porosity The as-printed films were not conductive and showed a relative area porosity of 38%. After pressing and sintering the porosity reduced by over 30% to 7% porous and demonstrated conductive behavior.

Bending tests were performed to analyze the adhesion of the printed film on the substrate and to quantify sample damage due to bending. Electrical resistance was used to quantify the flexibility and performance of the films as breakdown of the film due to cracks or delamination from the substrate would be detected as a rapid increase in resistance. The resistance of the films was measured in intervals over a series of 10,000 bending cycles and a 7.2% increase in resistance was observed over a 16 mm ROC. The low change in resistivity, combined with no sharp increase in resistance during the test, indicates good adhesion of the film to the substrate and high durability to bending.
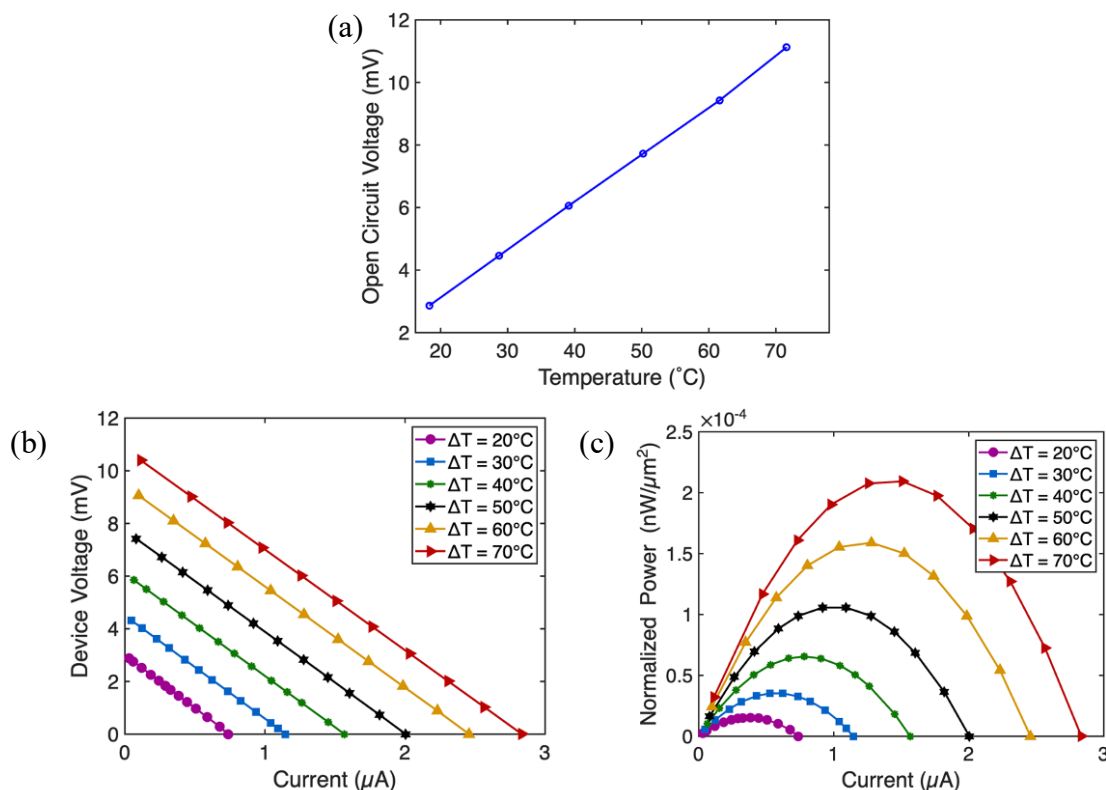
Figure 4.7   Electrical characterization of single leg TE film sintered at 425˚C. (a) VOC as a function of temperature difference, (b) device voltage as a function of current and (c) power curves normalized to cross sectional area for several temperature differentials

The output voltage and power of single TE films are shown in Figure 4.7 a-c.

Figure 4.7a shows the open circuit voltage (VOC) as a function of temperature

difference. The linear relationship of output voltage with temperature difference is due to

the Seebeck effect as $S = -\Delta V/\Delta T$. A maximum output voltage of 11 mV was observed at

a temperature difference of 70˚C. Device voltage and normalized power as a function of

electrical current for various temperature differences is shown in Figure 4.7 b,c. The

maximum power of the film is obtained when the external resistance, set by a variable

resistor, matches the internal resistance of the film. The power measurements were

normalized by the cross sectional area of the film, measured by optical microscope and

stylus profilometry to be 36495.7 μm^2. The maximum normalized power is 2.09 x 10^{-4} nw/μm^2 which corresponds to 7.64 nW for the 2 x 12 mm film. The electrical performance and superior flexibility of these films shows promise for flexible and low-power devices.

CHAPTER FIVE: CONCLUSIONS

5.1 Summary

The research goals of this work were to develop a PJP- compatible thermoelectric ink, demonstrate and optimize PJP of TE films, and optimize post-processing of the printed films. Bi_2Te_3 nanoflakes were produced using bottom up solvothermal synthesis. Synthesis conditions were successfully controlled to encourage formation of single nanopores in the center of the nanoflakes. Bi_2Te_3 ink was optimized in a cosolvent system for stability and particle size uniformity. PJP was performed on flexible polyimide substrates and print conditions were optimized for line thickness, uniformity, and minimal overspray. After printing the samples were mechanically pressed and thermally sintered to densify the films. Four different sintering conditions were tested and the impact on Seebeck Coefficient and electrical conductivity was measured. Finally, bending tests, electrical property measurements, and power measurements were performed on single films. This work marks a significant advancement to the fields of plasma jet printing for zero- gravity applications and fabrication of flexible thermoelectric generators.

Key findings include:

- The presence of nanopores dramatically increased the Seebeck coefficient compared to Bi_2Te_3 films with no nanopores, reaching values comparable with doped Bi_2Te_3.[92, 103]

- Mechanical pressing of as-printed films increased electrical conductivity and power factor compared to previous work of non-pressed AJP TE films.[92]

- PJP deposited TE films demonstrate excellent adhesion, with only 7.2% variation in resistance after 10,000 bending cycles over 16 mm ROC.

5.3 Future Work

Plasma Jet Printing Optimization

Calculation of the Reynolds, Ohnesorge, and Weber number of colloidal inks have been well characterized for inkjet printers, and advances have been made in optimizing these calculates for AJP.[94, 95] PJP is similar to AJP in terms of aerosolization of particles, however the plasma deposition complicates the direct application of AJP-optimized Reynolds number equations to PJP systems. In particular, accurate calculation of plasma velocity is needed to accurately calculate Reynolds number for PJP and relate it to print optimization.

Hot Injection Synthesis and Inkjet Printing

In this study as-synthesized Bi_2Te_3 nanoflakes had an average width of ~598 nm and a thickness of ~59 nm. We determined two major obstacles after initial attempts to formulate and print an IJP compatible Bi_2Te_3. First, the particles were not stable in the water, ethylene glycol, and isopropanol cosolvent ink solution used, causing particles to sediment out of the ink during printing and clog the printer cartridge. Second, the average particle size is much larger than previous demonstrations of inkjet printed inks, in which particles were in the range of 50 – 300 nm.[104] Solution stability has been addressed in part by the study performed for ink formulation for plasma jet printing in which a water,

ethylene glycol, and ethanol cosolvent system was determined to provide the best particle stability. However, further tuning of the contact angle and surface tension of this system will need to be optimized by varying the ratio of cosolvent components to formulate an IJP compatible ink.

The second obstacle is to reduce the lateral width of the nanoflakes to a size at or below 300 nm. In a standard synthesis process the Bi and Te precursor chemicals, reducing agent (NaOH), and capping agent (PVP) are combined with ethylene glycol before heating the entire solution to the synthesis temperature (190°C). In this process particle nucleation begins when the solution reaches ~160°C, as indicated by a visible color change in the reaction flask. As a result, the nucleation phase begins 30°C and ~20 minutes before the solution reaches the desired synthesis temperature of 190°C. To better observe the impact of synthesis time on particle nucleation without the influence of early nucleation we employed a hot injection synthesis method in which room temperature precursors were injected into a high temperature surfactant. Particle nucleation begins upon injection due to supersaturation of precursors. The room temperature precursor reduces the reaction temperature, resulting in termination of the nucleation stage and initiating the growth stage.[105]

The reducing agent and capping agent were combined with ethylene glycol and heated to 190°C. Bi and Te precursors were dissolved in ethylene glycol and injected into the surfactant solution and an immediate color change from clear and colorless to black was observed. Aliquots were removed from the reaction flask and quenched in an ice water bath after 1, 4, 6, 10, 15, 20, 30, 60, and 180 minutes to observe the nucleation

process. Figures 5.1a-i show AFM images of the observed morphology at each synthesis

time.
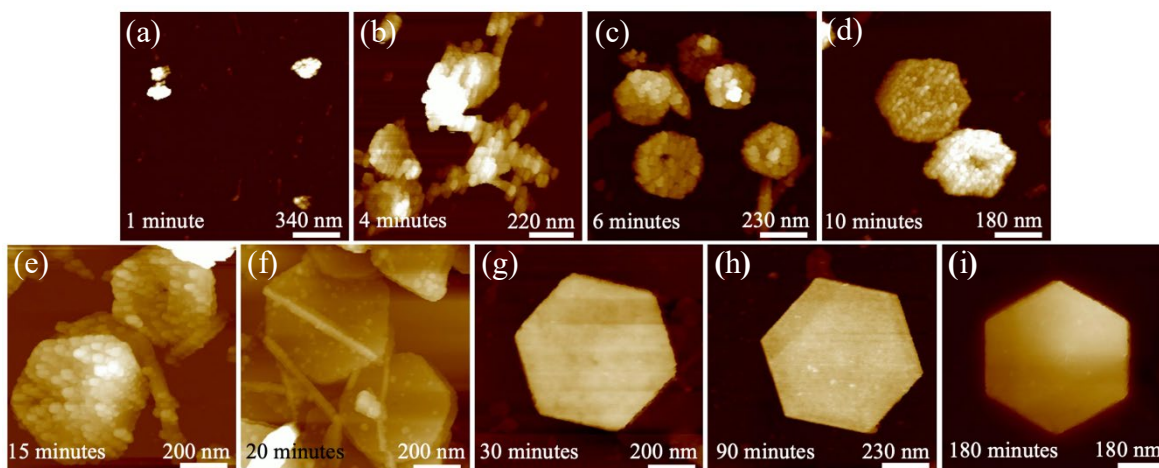
Figure 5.1   **AFM images showing morphology of Bi$_2$Te$_3$ nanoflakes synthesized at 190˚C for various times via hot injection.**

Particle agglomerations are observed at the shortest synthesis time and clear

hexagonal shaped nanoflakes appear after 6 minutes. Rough morphology, possibly from

adsorbed precursor, is observed on these nanoflakes up until the 20 minute mark, after

which crystalline nanoflakes are observed. Average width and thickness histograms are

shown in Figure 5.2a, b. Lateral width increases sharply after the 20 minute mark, and a

corresponding reduction in thickness is observed at the same time. Based on this work it

is proposed that Bi$_2$Te$_3$ nanoflakes synthesized via hot injection for 20 minutes are a

possible path forward for inkjet printing.
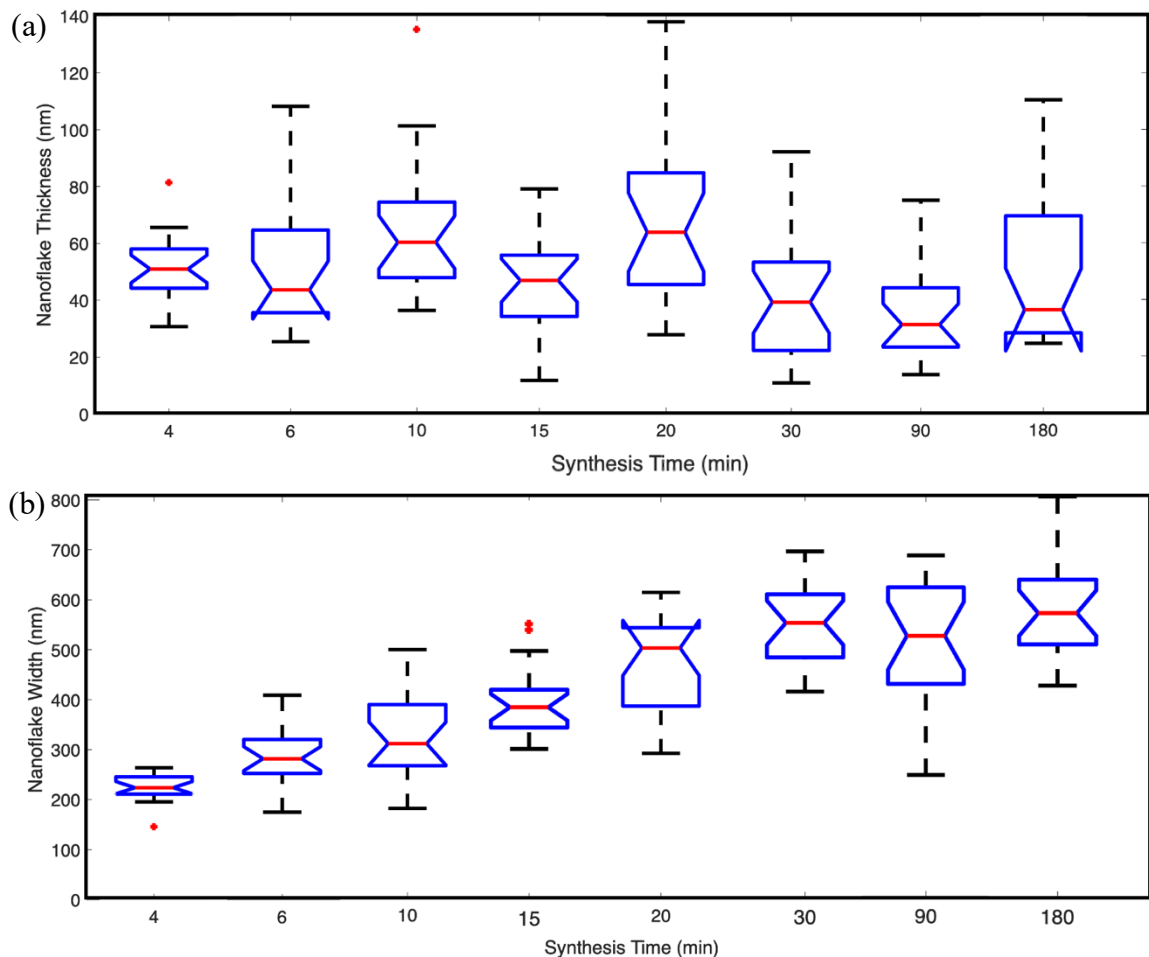
Figure 5.2   Distributions of (a) average thickness and (b) average width of Bi$_2$Te$_3$ nanoflakes synthesized via hot injection. Red line indicates median and wings upper and lower wings indicate 75th and 25th percentiles.

Temperature Controlled Hetero- and Nano- Structures

Nanoflake morphology has been observed to change depending on synthesis temperature. Recently, a few studies have reported synthesis of Bi$_2$Te$_3$- Te heterostructures in which a Bi$_2$Te$_3$ nanoflakes forms around a Te nanorod.[106–108] We have observed a similar heterostructure when the oil bath temperature of our standard Bi$_2$Te$_3$ was lowered to ~185˚C, as shown in Figure 5.3a. These types of heterostructures have demonstrated enhanced thermoelectric performance due to optimized reduced Fermi level and enhanced phonon scattering.[108]

The temperature dependent presence or absence of single nanopores in Bi_2Te_3

nanoflakes has also been observed recently.[60, 109] In addition to the observation of the

presence of nanoflakes, we have also observed what appears to be temperature-dependent

nanopore size, as shown in Figure 5.3 b, c. Nanoflakes synthesized in an oil bath at 190°C

(Figure 4.3b) show a pore diameter of ~100 nm while synthesis at ~205°C yields a pore

size of ~20 nm. The presence of single nanopores has been predicted to enhance

thermoelectric performance by acting as an additional phonon scattering site and

reducing thermal conductivity.[60, 109]

Further work regarding nanostructures includes additional synthesis experiments

with more accurate temperature control to better understand the formation of various

structures and the impact of temperature on nanopore diameter. In addition, studies

correlating synthesis temperature, nanopore diameter, and the impact on thermal
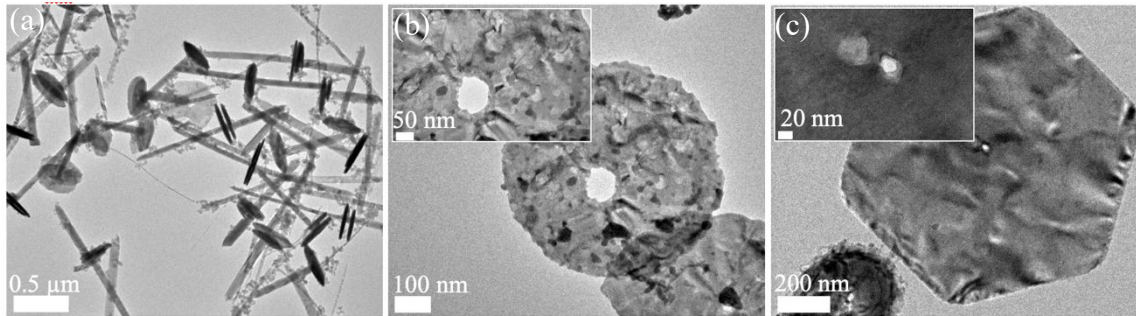
conductivity and ZT are recommended.

Figure 5.3   Morphology of Bi_2Te_3- based structures synthesized with oil bath temperature at (a) ~185°C, (b) ~190°C, (c) ~205°C.

REFERENCES

1. Energy Flow Charts: Charting the Complex Relationships Between Energy, Water, and Carbon. Lawrence Livermore National Laboratory and U.S. Department of Energy. https://flowcharts.llnl.gov/commodities/energy (2021).

2. Monthly Energy Review, Tables 1.3 and 11.1, preliminary data. U.S. Energy Information Administration. https://www.eia.gov/energyexplained/energy-and-the-environment/where-greenhouse-gases-come-from.php (2021).

3. Halkos, G. E., & Gkampoura, E. C. Reviewing Usage, Potentials, and Limitations of Renewable Energy Sources. *Energies* **13**, 2906 - 2925 (2020).

4. Burenet, N. V. *et al*. Review of thermoelectric generation for internal combustion engine waste heat recovery. *PECS* **91**,101009 (20220.

5. Crane, D. T., & Lagrandeur, J. W. Progress Report on BSST-Led US Department of Energy Automotive Waste Heat Recovery Program. *J. Electron. Mater* **39**, 2142 – 2148 (2010).

6. Espinosa, N. *et al*. Modeling a Thermoelectric Generator Applied to Diesel Automotive Heat Recovery. *J. Electron. Mater* **39**, 1446 – 1455 (2010).

7. Zhang, Y. *et al*. High-temperature and high-power-density nanostructured thermoelectric generator for automotive waste heat recovery. *Energy Convers. Manag.* **105**, 946 – 950 (2015).

8. Kempf, N., & Zhang Y. Design and optimization of automotive thermoelectric generators for maximum fuel efficiency improvement. *Energy Convers. Manag*. **121**, 224 – 231 (2016).

9. Rowe, D. M. Applications of nuclear-powered thermoelectric generators in space. *App. Energy* **40**, 241 – 271 (1991).

38

10. Holgate, T. C. *et al*. Increasing the Efficiency of the Multi-Mission Radioisotope Thermoelectric Generator. *J. Electron. Mater* **44**, 1814 – 1821 (2015).

11. Ambrosi, R. M. *et al*. European Radioisotope Thermoelectric Generators (RTGs) and Radioisotope Heater Units (RHUs) for Space Science and Exploration. *Space Sci. Rev* **215**, 1 – 41(2019).

12. Liu, K. *et al*. Experimental optimization of small-scale structure-adjustable radioisotope thermoelectric generators. *Appl. Energy* **280**, 115907 (2020).

13. Kraemer, D. *et al*. High- performance flat-panel solar thermoelectric generators with high thermal concentration. *Nat. Mater.* **10**, 532 – 538 (2011).

14. Baranowski, L. L., Snyder, G. J., & Toberer, E. S. Concentrated solar thermoelectric generators. *Energy Environ. Sci.* **5**, 9055 (2012).

15. Sundarraj, P. *et al*. Recent advances in thermoelectric materials and solar thermoelectric generators- a critical review. *RSC Adv.* **4**, 46860 (2014).

16. Kraemer, D. *et al*. Concentrating solar thermoelectric generators with a peak efficiency of 7.4%. *Nat. Energy* **1**, 16153 (2016).

17. Siddique, A. R. M., Mahmud, S., Van Heyst, B. A review on the state of the science on wearable thermoelectric power generators (TEGs) and their existing challenges. *Renew. Sust. Energ. Rev.* **73**, 730 – 744 (2017).

18. Hyland, M. *et al*. Wearable thermoelectric generators for human body heat harvesting. *Appl. Energy* **182**, 518 – 524 (2016).

19. Wang, Z. *et al*. Realization of a wearable minitiarized thermoelectric generator for human body applications. *Sens Actuators A Phy* **156**, 95 – 102 (2009).

20. Nozariasbmarz, A. *et al*. Review of wearable thermoelectric energy harvesting: From Body temperature to electronic systems. *Appl. Energy* **258**, 114069 (2020).

21. Chen, M. *et al*. Energy efficiency analysis and impact evaluation of the application of thermoelectric power cycle to today's CHP systems. *Appl. Energy* **87**, 1231 – 1238 (2010).

22. Montecucco, A., Siviter, J., Knox, A. R. Combined heat and power system for stoves with thermoelectric generators. *Appl. Energy* **185**, 1336-1342 (2017).

23. Champier, D. Thermoelectric generators: A review of applications. *Energy Convers. Manag.* **140**, 167-181 (2017).

24. Li, G. N. *et al*. Miniature self-powering and self-aspirating combustion-powered thermoelectric generator burning gas fuels for combined heat and power supply. *J. Power Sources* **506**, 230263 (2021).

25. Jaziri, N. *et al*. A comprehensive review of Thermoelectric Generators: Technologies and common applications. *Energy Rep.* **6**, 264 – 287 (2020).

26. Sootsman, J. R., Chung, D. Y., Kanatzidis, M. G. New and Old Concepts in Thermoelectric Materials. *Angew. Chem. Int. Ed.* **48**, 8616 – 8639 (2009).

27. Tan, G., Zhao, L. -D., Kanatzidis, M. G. Rationally Designing High-Performance Bulk Thermoelectric Materials. *Chem. Rev.* **116**, 12123 – 12149 (2016).

28. Ma, Z. *et al.* Review of experimental approaches for improving ZT of thermoelectric materials. *Mater Sci Semicond* **121**, 105303 (2016).

29. Cai, B. *et al*. Promising materials for thermoelectric applications. *J. of Alloys Compd* **806**, 471 – 486 (2019).

30. Saberi, Y., Sajjadi, S. A. A comprehensive review on the effects of doping process on the thermoelectric properties of Bi2Te3 based alloys. *J. Alloys Compd* **904**, 163918 (2022).

31. Biswas, K. *et al*. High-performance bulk thermoelectrics with all-scale hierarchical architectures. *Nature* **489**, 414 – 418 (2012).

32. Dresselhaus, M. S. *et al.* New Directions for Low-Dimensional Thermoelectric Materials. *Adv. Mater* **19**, 1043 – 1053 (2007).

33. Poudel, B. *et al*. High-Thermoelectric Performance of Nanostructured Bismuth Antimony Telluride Bulk Alloys. *Sci* **320**, 634 – 638 (2008).

34. Minnich, A. J. *et al*. Bulk nanostructured thermoelectric materials: current research and future prospects. *Energy Environ. Sci* **2**, 466 – 479 (2009).

35. Zulkepli, N. *et al*. Review of Thermoelectric Generators at Low Operating Temperatures: Working Principles and Materials. *Micromachines* **12**, 734 – 759 (2021).

36. Chen, X. *et al*. Enhanced Thermoelectric Performance of $Bi_2Te_{2.7}Se_{0.3}/Bi_2S_3$ Synthesized by Anion Exchange Method. *RRL* **14**, 1900679 (2020).

37. Chen, X. *et al*. Enhanced thermoelectric properties of n-type $Bi_2Te_{2.7}Se_{0.3}$ for power generation. *J. Mater. Sci. Mater* **31**, 4924 – 4930 (2020).

38. Nozariasbmarz, A. *et al*. Thermoelectric generators for wearable body heat harvesting: Material and device concurrent optimization. *Nano Energy* **67**, 104265 (2020).

39. Lei, J. *et al*. Engineering electrical transport in α- MgAgSb to realize high performances near room temperature. *Phys. Chem. Chem. Phys.* **24***, 16729 (2018)*.

40. Wu, Y. *et al* P. Thermoelectric Enhancements in PbTe Alloys Due to Dislocation-Induced Strains and Converged Bands. *Adv. Sci. Lett.* **7**, 1902628 (2020).

41. Zong, P. *et al*. Skutterudite with graphene-modified grain-boundary complexion enhances ZT enabling high-efficiency thermoelectric device. *Energy Environ. Sci.* **10**, 183 – 191 (2017).

42. Xing, Y. *et al*. High-efficiency half- Heusler thermoelectric modules enabled by self-propagating synthesis and topologic structure optimization. *Energy Environ. Sci.* **12**, 3390 – 3399 (2017).

43. Li, Y. *et al*. Enhancing thermoelectric properties of p-type SiGe by SiMo addition. *J. Mater. Sci. Mater* **30**, 9163 – 9170 (2019).

44. Wang, J. *et al*. Enhanced Thermoelectric Performance in n-type SrTiO3/ SiGe Composite. *ACS Appl. Mater. Interfaces* **12**, 2687 – 2694 (2020).

45. Witting, I. T. *et al.* The Thermoelectric Properties of Bismuth Telluride. *Adv. Electron. Mater.* **5**, 1800904 (2019).

46. An, J. *et al.* Synthesis of heavily Cu- doped Bi_2Te_3 nanoparticles and their thermoelectric properties. *J. of Solid State Chem* **270**, 407 – 412 (2019). DOI: 10.1016/j.jssc.2018.11.024

47. Li, F. *et al.* High thermoelectric properties achieved in environmentally friendly sulfide compound Bi_2SeS_2 by nanoengineering. *Nano Energy* **88**, 106273 (2021).

48. Malik, I. *et al.* Enhanced thermoelectric performance of n-type Bi_2Te_3 alloyed with low cost and highly abundant sulfur. *Mater. Chem. and Phys.* **255**, 123598 (2020).

49. Singh, N. K. *et al.* Charge carriers modulation and thermoelectric performance of intrinsically p-type Bi_2Te_3 by Ge doping. *J. Alloys Compd* **746**, 350 – 355 (2018).

50. Zhang, C. *et al.* Controlled growth of bismuth antimony telluride $Bi_xSb_{2-x}Te_3$ nanoplatelets and their bulk thermoelectric nanocomposites. *Nano Energy* **15**, 688 – 696 (2015).

51. Martín-González, M. S. *et al.* Insights into the Electrodeposition of Bi_2Te_3. *J. Electrochem. Soc.* **149**, C546 – C554 (2002).

52. H. Mamur, H. *et al.* A review on bismuth telluride (Bi_2Te_3) nanostructure for thermoelectric applications. *Renew. Sust. Energ. Rev.* **82**, 4159 – 4169 (2018).

53. Gao, M. -R. *et al.* Nanostructured metal chalcogenides: synthesis, modification, and applications in energy conversion and storage devices. *Chem. Soc. Rev.* **42**, 2986 – 3017 (2013).

54. Prieto, A. L. *et al.* Electrodeposition of Ordered Bi_2Te_3 Nanowire Arrays. *JACS* **123**, 7160 – 7161 (2001).

55. Ashalley, E. *et al.* Bismuth telluride nanostructures: preparation, thermoelectric properties and topological insulating effect. *Front. Mater. Sci.* **9**, 103 – 125 (2015).

56. Y. Zhang, Y. *et al.* High Yield Bi_2Te_3 Single Crystal Nanosheets with Uniform Morphology via a Solvothermal Synthesis. *Cryst. Growth Des* **13**, 645 – 651 (2013).

57. Im, H. J. *et al*. Solvothermal Synthesis of Sb_2Te_3 nanoplates under various synthetic conditions and their thermoelectric properties. *Appl. Surf. Sci.* **475**, 510 – 514 (2019).

58. Akshay, V. R. *et al*. Surfactant-Induced Structural Phase Transitions and Enhanced Room Temperature Thermoelectric Performance in n-Type Bi_2Te_3 Nanostructures Synthesized via Chemical Route. ACS *Appl. Nano Mater.* **1**, 3236 – 3250 (2018).

59. Akshay, V. R., Suneesh, M. V., Vasundhara, M. Tailoring Thermoelectric Properties through Structure and Morphology in Chemically Synthesized n-Type Bismuth Telluride Nanostructures. *Inorg. Chem.* **56**, 6264 – 6274 (2017).

60. Hosokawa, Y., Tomita, K., Takashiri, M. Growth of single-crystalline Bi_2Te_3 hexagonal nanoplates with and without single nanopores during temperature-controlled solvothermal synthesis. *Sci. Rep.* **9**, 10790 (2019).

61. Committee F42 A. F2792-12a: Standard Terminology for Additive Manufacturing Technologies (2012).

62. Kruth, J. -P., Leu, M. C., Nakagawa, T. Progress in Additive Manufacturing and Rapid Prototyping. *CIRP Annals Manuf Technol* **47**, 525 – 540 (1998).

63. Ngo, T. D. *et al*. Additive manufacturing (3D printing): a review of materials, methods, applications and challenges. *Compos. B Eng.* **143**, 172 – 196 (2018).

64. Uriondo, A. *et al*. The present and future of additive manufacturing in the aerosopcae sector: A review of important aspects. *J. Aerosp. Eng.* **229**, 2132 – 2147 (2015).

65. Wiese, M., Thiede, S., Herrmann, C. Rapid manufacturing of automotive polymer series parts: A systematic review of processes, materials and challenges. *Addit. Manuf.* **36**, 101582 (2020).

66. Guo, N., Leu, M. C. Additive manufacturing: technology, applications and research needs. *Front. Mech. Eng.* **8**, 215 – 243 (2013).

67. Najmon, J. C., Raeisi, S., Tovar, A. Review of additive manufacturing technologies and applications in the aerospace industry. *Additive Manufacturing for the Aerospace Industry*, 7-31 (2019).

68. Khan Y. *et al*. A New Frontier of Printed Electronics: Flexible Hybrid Electronics. *Adv. Mater* **32**, 1905279 (2020).

69. Burton, M. *et al*. Printed Thermoelectrics. *Adv. Mater* **51**, 2108183 (2022).

70. Corzo, D., Tostado-Blázquez, G., Baran, D. Flexible Electronics: Status, Challenges, and Opportunities. *Front. Electron.* **1**, 594003 (2020).

71. Pagliaro, M., Ciriminna, R., Palmisano, G. Flexible Solar Cells. *Chem Sus Chem* **1**, 880-891. (2008).

72. Mitra, K. Y. *et al*. Manufacturing of All Inkjet- Printed Organic Photovoltaic Cell Arrays and Evaluating their Suitability for Flexible Electronics. *Micromachines*, **9**, 642 – 662 (2018).

73. Huang, L. *et al*. Graphene- Based Conducting Inks for Direct Inkjet Printing of Flexible Conductive Patterns and Their Applications in Electric Circuits and Chemical Sensors. *Nano Res.* **4**, 675 – 684 (2011).

74. Wang, X. *et al*. Inkjet-printed flexible sensors: From function materials, manufacture process, and applications perspective. *Mater. Today Commun.* **31**, 103263 (2022).

75. Salaoru, I., Maswoud, S., Paul, S. Inkjet Printing of Functional Electronic Memory Cells: A Step Forward to Green Electronics. *Micromachines* **10***, 417 – 427 (2019).

76. Grubb, P. M. *et al*. Inkjet Printing Of High Performance Transistors With Micron Order Chemically Set Gaps. *Sci. Rep.* **7**, 1202 – 1210 (2017).

77. Fujimoto, K. T. *et al*. Aerosol jet printed capacitive strain gauge for soft structural materials. *npj Flex. Electron.* **4**, 32 – 41 (2020).

78. Pandhi, T. *et al*. Fully inkjet-printed multilayered graphene-based flexible electrodes for repeatable electrochemical response. *RCS Adv.* **10**, 38205 (2020).

79. Ou, C. *et al*. Enhanced thermoelectric properties of flexible aerosol-jet printed carbon nanotube-based nanocomposites. *APL Mater.* **6**, 096101 (2018).

80. Hossain, M. S. *et al*. Recent advances in printable thermoelectric devices: materials, printing techniques, and applications. *RSC Adv.* **10**, 8421 – 8434 (2020).

81. Dimatix Materials Printer DMP-2850. Fujifilm Dimatix, https://asset.fujifilm.com/www/us/files/2021-04/c80cdd17080a06095c34a26d6221c81a/PDS00085.pdf (2021).

82. Aerosol Jet 200 Series Systems. Optomec, https://www.optomec.com/wp-content/uploads/2014/08/AJ_200_WEB_0216.pdf (2016).

83. Sher, D. Antenna and sensor components get plasma jet printed in microgravity. 3D Printing Media Network, https://www.3dprintingmedia.network/antenna-and-sensor-components-get-plasma-jet-printed-in-zero-gravity/ (2021).

84. Dey, A. *et al*. Plasma jet based *in situ* reduction of copper oxide in direct write printing. *J. Vac. Sci. Technol.* **37**, 31203 (2019).

85. Gandhiraman, R. P. *et al*. Plasma jet printing for flexible substrates *Appl. Phys. Lett.* **108**, 123103 (2016).

86. Gandhiraman, R. P. *et al*. Plasma Jet Printing of Electronic Materials on Flexible and Nonconformal Objects *ACS Appl. Mater. Interfaces* **6**, 20860 (2014).

87. Selwyn, G. S. *et al*. Materials Processing Using an Atmospheric Pressure, RF-Generated Plasma Source. *Contrib. to Plasma Phys.* **41**, 610 – 619 (2001).

88. Teschke, M. *et al*. High- Speed Photographs of a Dielectric Barrier Atmospheric Pressure Plasma Jet. *IEEE Trans Plasma Sci IEEE* **33**, 310 – 311 (2005).

89. Ramamurti, R. *et al*. Atmospheric Pressure Plasma Printing of Nanomaterials for IoT Applications. *OJ-Nano* **1**, 47 – 56 (2020).

90. Wang, Y. *et al*. Plasma jet printing for preparation of N-doped graphene electrodes. *J. Mater. Sci. Mater.* **30**, 8944 – 8954 (2019).

91. Dey, A. *et al*. Plasma Jet Printing and *in* Situ Reduction of Highly Acidic Graphene Oxide. *ACS Nano* **12**, 5473 – 5481 (2018).

92. Hollar, C. *et al*. High-Performance Flexible Bismuth Telluride Thin Film from Solution Processed Colloidal Nanoplates. *Adv. Mater. Technol.* **5**, 2000600 (2020).

93. Feng, J. Q., Renn, M. J. Aerosol Jet Direct-Write for Microscale Additive Manufacturing. *J. Micro Nanomanuf* **7**, 011004-1 – 011004-7 (2019).

94. Feng, J. Q., Ramm, A., Renn, M. J. A quantitative analysis of overspray in Aerosol Jet printing. *Flex. Print.* **6**, 045006 (2021).

95. Feng, J. Q. Mist flow visualization for round jets in Aerosol Jet Printing. *Aerosol Sci. Technol.* **53**, 45 – 52 (2019).

96. Derby, B. Inkjet Printing of Functional and Structural Materials: Fluid Property Requirements, Feature Stability, and Resolution. *Annu. Rev. Mater. Res.* **40**, 395 – 414 (2010).

97. McKinley, G. H., Renardy, M. Wolfgang von Ohnesorge. *Phys. Fluids* **23**, 127101 (2011).

98. Jin, D. J, Uhm, H. S., Cho, G. Influence of the gas-flow Reynolds number on a plasma column in a glass tube. *Phys. Plasmas.* **20**, 083513 (2013).

99. Pinchuk, M. *et al* in. Propagation of atmospheric pressure helium plasma jet into ambient air at laminar gas flow. *J. Phys. Conf.* **830**, 012060 (2016).

100. Wang, R. *et al*. Laminar-to-Turbulent Transition of a DC Helium/ Oxygen (2%) Plasma Microjet. *IEEE Trans. Plasma Sci. IEEE* **39**, 2374 – 2375 (2011).

101. Whalley, R. D., Walsh, J. L. Turbulent jet flow generated downstream of a low temperature dielectric barrier atmospheric pressure plasma device. *Sci. Rep.* **6**, 31756 (2016).

102. Subrati, A. *et al* Y. Monitoring the multiphasic evolution of bismuth telluride nanoplatelets. *Cryst. Eng. Comm.* **22**, 7918 – 7928 (2020).

103. Varghese, T. *et al*. High-performance and flexible thermoelectric films by screen printing solution-processed nanoplate crystals. *Sci. Rep.* **6**, 33135 (2016).

104. Pandhi, T. *et al*. Fully inkjet-rinted multilayered graphene-based flexible electrodes for repeatable electrochemical response. *RSC* **10**, 38205 – 38219 (2020).

105. Carey, G. H. *et al*. Colloidal Quantum Dot Solar Cells. *Chem. Rev.* **115**, 12732 – 12763 (2015).

106. Cheng, L. *et al*. T-Shaped Bi_2Te_3-Te Heteronanojunctions: Epitaxial Growth, Structural Modeling, and Thermoelectric Properties. *Am. J. Phys. Chem.* **117**, 12458 – 12464 (2013).

107. Zhang, Y. *et al* H. Rational design and controlled synthesis of Te/ Bi_2Te_3 heterostructure nanostring composites. *J. Cryst. Growth* 421, 13 – 18 (2015).

108. Hong, M. *et al*. Enhancing thermoelectric performance of Bi_2Te_3- based nanostructures through rational structure design. *Nanoscale* **8**, 8681 – 8686 (2016).

109. Dun, C. *et al*. Bi_2Te_3 Plates with Single Nanopore: The Formation of Surface Defects and Self-Repair Growth. *Chem. Mater.* **30**, 1965 – 1970 (2018).